Journal of Solid State Chemistry 182 (2009) 3312–3319

Contents lists available at ScienceDirect

Journal of Solid State Chemistry

journal homepage: www.elsevier.com/locate/jssc

Structural characterization of C–S–H and C–A–S–H samples—Part I: Long-range order investigated by Rietveld analyses

Guillaume Renaudin [a,d,*], Julie Russias [b], Fabrice Leroux [c,d], Fabien Frizon [b], Céline Cau-dit-Coumes [b]

[a] Clermont Université, Ecole Nationale Supérieure de Chimie de Clermont-Ferrand, LMI, BP 10448, F-63000 Clermont-Ferrand, France
[b] Commissariat à l'Energie Atomique, DEN, Marcoule, Waste Treatment and Conditioning Research Department, F-30207 Bagnols sur Cèze, France
[c] Clermont Université, UBP, Laboratoire des Matériaux Inorganiques, F-63000 Clermont-Ferrand, France
[d] CNRS, UMR 6002, F-63177 Aubière Cedex, France

ARTICLE INFO

Article history:
Received 19 May 2009
Received in revised form
16 September 2009
Accepted 20 September 2009
Available online 30 September 2009

Keywords:
C–S–H
C–A–S–H
Tobermorite
Powder X-ray diffraction
Rietveld analysis

ABSTRACT

Rietveld analyses on samples belonging to C–S–H and C–A–S–H series ($0.8 \leq C/S \leq 1.7$) were realized on X-ray powder patterns. The tobermorite M model was successfully used to refine all the powder patterns from C–S–H samples whatever the C/S value. This gives clear indication on the steady change in a unique structural description, corresponding to a 'tobermorite M defect' model, when passing from C–S–H(I) ($C/S < 1.0$) to C–S–H(II) type ($C/S > 1.0$). The possibility for both C–S–H types (from polymerized silicate chains to isolated silicate dimers) to accommodate the same structural model is explained by the continuous evolution of the occupancies of the cationic sites: the interlayer Ca atoms, the Si atoms from paired and bridging silicates. Accurate refinements of the structural and microstructural parameters evidenced the well crystallized feature of C–S–H phase combined with a small coherent domain size. Insertion of Al atoms in the C–S–H structure (C–A–S–H phase) involves a clear disruption into the layered atomic framework. The large increase of layer spacing observed when incorporating aluminum into C–S–H indicates that Al atoms should be located in the interlayer region of the structure in new crystallographic sites. Aluminum atoms are not substituted silicon crystallographic sites or interlayer calcium crystallographic sites.

1. Introduction

Calcium Silicate Hydrate (C–S–H) is known to be the primary binding phase in Portland cement. Since late 19th century, the first studies were devoted to understand the setting and hardening of hydrated Portland cement [1–3]. C–S–H has been quickly identified as the principal binding phase. Its chemical composition has been subject to numerous studies [4–7]. However, difficulties to characterize the calcium silicate phase arose mainly from its poorly crystalline feature. Nevertheless two C–S–H types have been identified, respectively, named C–S–H(I) and C–S–H(II), according to their Ca/Si ratio [8], respectively, low (below 1.0) and high (above 1.0). According to Taylor C–S–H(I) and C–S–H(II) derive, respectively, from a tobermorite model and the jennite model [8,9]. More recently, Nonat proposed a different nomenclature based on solution equilibrium data with the existence of three different phases: α-C–S–H ($0.66 < Ca/Si < 1.0$), β-C–S–H ($1.0 < Ca/Si < 1.5$) and γ-C–S–H ($1.5 < Ca/Si < 2.0$) [10]. In 2008, Richardson has written a comprehensive review on the different structural models proposed by number of authors the last fifty-year [11]. C–S–H phase has a layered structure and a fibrous microstructure. X-ray powder patterns of C–S–H show similarities to tobermorite, a rare crystalline calcium silicate hydrate mineral which has the approximate chemical composition $Ca_4(Si_6O_{18}H_2)\cdot Ca\cdot 4H_2O$ (i.e. a Ca/Si ratio of 0.83) first described in 1956 [12]. The tobermorite structure contains layers of sevenfold coordinated (monocapped trigonal prisms) Ca^{2+} ions (labeled Ca_L in the text) linked on both sides to linear silicate chains of the 'dreierkette' form in such a way as to repeat a kinked pattern after every three tetrahedra (see Fig. 1). Two of the three tetrahedra, named paired tetrahedra (usually labeled Si_P), are linked together and share O–O edges with the central Ca–O part of the layer. The third tetrahedron, named bridging tetrahedron (usually labeled Si_B), shares an oxygen atom at the pyramidal apex of a Ca polyhedron and connects the dimers of paired tetrahedra. Additional calcium atoms (labeled Ca_I in the text) are inserted in the interlayer region of the structure. The Ca/Si ratio can increase by removing some bridging tetrahedra (decrease of the Si content) with the concomitant replacement by interlayer Ca atoms (increase of Ca content) [13]. Several structural types have been solved for crystalline tobermorite. By considering the interlayer distance,

* Corresponding author at: Clermont Université, Ecole Nationale Supérieure de Chimie de Clermont-Ferrand, LMI, BP 10448, F-63000 Clermont-Ferrand, France. Fax: +33 4 73 40 71 08.
E-mail address: guillaume.renaudin@ensccf.fr (G. Renaudin).

0022-4596/$ - see front matter © 2009 Elsevier Inc. All rights reserved.
doi:10.1016/j.jssc.2009.09.026

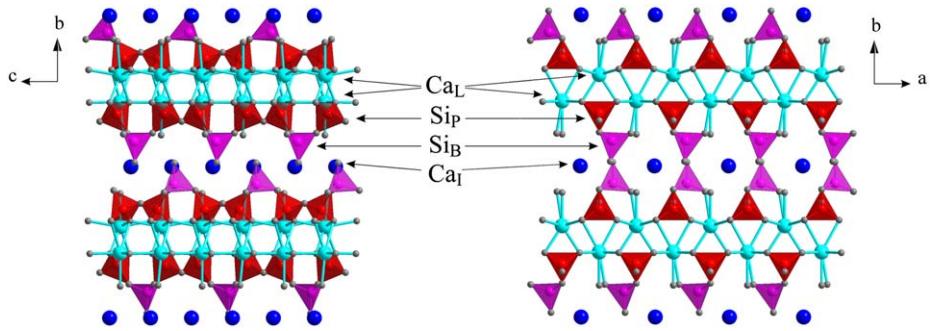

Fig. 1. Two projections (right: along the $\vec{a}$ axis; left: along the $\vec{c}$ axis) of the tobermorite M structural model given by Hamid [17]; using the conventional $\vec{b}$ unique monoclinic axis. Label Ca_L refers to layer calcium sites (i.e. the Ca1, Ca2, Ca3 and Ca4 crystallographic sites, seven coordinated light blue spheres), Ca_I refers to interlayer calcium sites (i.e. the Ca5 and Ca6 crystallographic sites, blue spheres), Si_P refers to the paired silicon tetrahedra (i.e. the Si1, Si2, Si4 and Si6 crystallographic sites, red tetrahedra) and Si_B refers to the bridging silicon tetrahedra (i.e. the Si3 and Si5 crystallographic sites, pink tetrahedra). (For interpretation of the references to the color in this figure legend, the reader is referred to the web version of this article).

Table 1
Starting material amounts and calculated compositions of the synthesized phases.

	Nominal composition: Ca/Si ratio					
	0.8	1.0	1.1	1.3	1.5	1.7
C–S–H						
CaO (mmol)	41.25	45.71	47.86	51.96	55.18	58.03
SiO_2 (mmol)	49.83	45.67	43.66	39.83	36.83	34.17
Solution (mL)	265.14	265.19	265.04	265.10	265.25	265.02
Experimental Ca/Si ratio[a]	0.82	0.98	1.08	1.24	1.40	1.59
Water amount[b] (%)	14.6	20.5	19.8	19.3	21.7	20.8
Composition[c]	$C_{0.8}SH_{1.0}$	$C_{1.0}SH_{1.7}$	$C_{1.1}SH_{1.7}$	$C_{1.2}SH_{1.7}$	$C_{1.4}SH_{2.1}$	$C_{1.4}SH_{1.9}$
C–A–S–H						
CaO (mmol)	16.95	21.19	23.30	27.54	31.78	36.01
SiO_2 (mmol)	21.17	21.17	21.17	21.17	21.17	21.17
Al_2O_3 (mmol)	1.06	1.06	1.06	1.06	1.06	1.06
Solution (mL)	500	500	500	500	500	500
Experimental Ca/(Si+Al) ratio[a]	0.71	0.82	0.92	1.04	1.17	1.24
Experimental Al/Si ratio[a]	0.10	0.10	0.10	0.10	0.10	0.10
Experimental Ca/Si ratio[a]	0.78	0.90	1.01	1.14	1.29	1.36
Water amount[b] (%)	22.6	20.2	20.5	19.4	19.6	19.7
Composition[c]	$C_{0.7}A_{0.05}S_{0.9}H_{1.6}$	$C_{0.8}A_{0.05}S_{0.9}H_{1.5}$	$C_{0.9}A_{0.05}S_{0.9}H_{1.6}$	$C_{1.0}A_{0.05}S_{0.9}H_{1.5}$	$C_{1.2}A_{0.05}S_{0.9}H_{1.7}$	$C_{1.2}A_{0.05}S_{0.9}H_{1.6}$

C_3A saturated solution with [Ca]=5.24 mmol L^{-1} and [Al]=4.24 mmol L^{-1}.

[a] Verified indirectly by chemical analysis of the solutions.

[b] Total weight loss determined by TGA analyses between room temperature and 1100 °C.

[c] Composition of the C–S–H (C–A–S–H) phases; taken into account the experimental Ca/Si ratio (Ca/(Si+Al) ratio) and the thermal contribution of the secondary $Ca(OH)_2$ (C–S–H_1.5 and C–S–H_1.7 samples) and $C_4A\overline{C}H_{11}$ (C–A–S–H_1.7 sample) phases.

three main tobermorite families are distinguished: the tobermorite 14, 11 and 9 Å. The two tobermorite 14 and 11 Å families are compatible with the interlayer distance observed in C–S–H formed in hardened Portland cement [14]. Amongst these two families, nine different structural types were described: tobermorite 14 Å [15], tobermorite 11 Å Mdo1 [16], tobermorite 11 Å Mdo2 [16], tobermorite O [17], tobermorite M [17] and four clinotobermorite types [18–20]. Due to the poorly resolved X-rays powder patterns of C–S–H in hardening cement pastes, its characterization has been mainly and largely realized by ^{29}Si NMR spectroscopy during the last twenty years [21–26]. Most studies agree that, upon composition change, a continuous structural evolution occurs between the two previously described C–S–H(I) and C–S–H(II) types. This paper presents a comprehensive Rietveld analysis realized from Laboratory X-rays powder diffraction patterns to investigate the structural features of C–S–H and C–A–S–H samples with a Ca/Si, or Ca/(Si+Al), ratio ranging from 0.8 to 1.7. The results support the tobermorite M-like structure. The apparent lack of long-range order in C–S–H is attributed to the nanometric size of the coherent domains rather than to a poorly ordered or quite amorphous compound. However, the insertion of aluminum into C–S–H to form C–A–S–H leads to the formation of a poorly crystallized material coming from a highly disorganized stacking sequence.

2. Experimental

2.1. C–S–H and C–A–S–H syntheses

C–S–H_*n* samples with n, the nominal Ca/Si atomic ratio,=0.8, 1.0, 1.1, 1.3, 1.5 and 1.7 were synthesized from silica (Degussa, Aerosil 380) and calcium oxide (Aldrich, 99.9% pure) freshly decarbonated 3 h at 900 °C. Demineralized and decarbonated water added to reach a water/solid ratio of 50.

C–A–S–H_n samples with a nominal Al/Si atomic ratio of 0.1 and a nominal Ca/Si atomic ratio *n*=0.8, 1.0, 1.1, 1.3, 1.5 and 1.7 were synthesized from silica (Degussa, Aerosil 380) and calcium oxide (Aldrich, 99.9% pure) freshly decarbonated for 3 h at 900 °C

incorporated in a saturated solution of tricalcium aluminate (C_3A 1 g. L^{-1} in demineralized and decarbonated water) following the method proposed by Chen et al. [27] Calcium and aluminum concentrations in the solution were determined by ICP-AES; respectively, 210.0 and 114.4 mg L^{-1}. Silica and calcium oxide were incorporated in these filtered solutions (filtered at 0.45 μm) to reach a water/solid ratio of 50, a Al/Si atomic ratio of 0.1 and the six Ca/(Al+Si) ratios from 0.8 to 1.7.

All the suspensions, from both C–S–H and C–A–S–H syntheses, were stored at 20 °C under N_2 atmosphere for three weeks under stirring in closed polypropylene bottles. They were then filtered under nitrogen and rinsed with acetone. The precipitates were subsequently dried in a desiccator, under slight vacuum, over silica gel, at room temperature. Experimental conditions are summarized in Table 1.

2.2. Analytical techniques

2.2.1. Powder X-Ray Diffraction (PXRD) and Rietveld analyses

Powder X-ray diffraction (PXRD) patterns were recorded on a X'Pert Pro PANalytical diffractometer, θ–θ geometry, equipped with a X-Celerator solid detector and using Cu$K\alpha$ radiation (λ=1.54184 Å). Powder patterns were recorded at room temperature in the interval $3^\circ < 2\theta < 60^\circ$, with a step size of $\Delta 2\theta = 0.01745^\circ$ and a counting time of 200 s per step. A total counting time of about 100 min was used for each sample. Si powder pattern was collected (from pure silicon powder) by using the same experimental conditions in order to extract the instrumental resolution function. The low resolutions of the X-ray powder patterns are intrinsic to the samples and are not diffractometer dependent. Then an increase of the two theta range or of the counting time did not allowed to improve the quality of the data before performing the Rietveld analyses.

Rietveld refinements were performed with the FullProf program [28]. The following tobermorite-like structures, as well as the triclinic $P\bar{1}$ jennite structure (ICSD No. 151413 [29]), were successively considered to refine the X-ray powder patterns: tobermorite 14 Å with the monoclinic *Cc* symmetry (ICSD No. 152489 [15]), tobermorite 11 Å Mdo1 with the orthorhombic *Fdd*2 symmetry (ICSD No. 92941 [16]), tobermorite 11 Å Mdo2 with the monoclinic *Cm* symmetry (ICSD No. 92942 and 92943 [16], and related ICSD No. 87690 [18]), tobermorite O with the orthorhombic *Imm*2 symmetry (ICSD No. 100405 [17]), tobermorite M with the monoclinic $P2_1$ symmetry (ICSD No. 40048 [17]), and four clinotobermorite types; 1/with the monoclinic $C2/c$ symmetry (ICSD No. 56854 [19]), 2/with the monoclinic $C2/m$ symmetry (ICSD No. 403090 [20]), 3/with the monoclinic *Cc* symmetry (ICSD No. 90036 [19]), 4/with the triclinic *P*1 symmetry (ICSD Nos. 90035, 90034 [19]). Both structural and microstructural parameters were refined. The use of the instrumental resolution function allowed the extraction of the sample intrinsic average apparent crystallite size. The diffraction profiles (both instrumental and sample intrinsic) were modeled by using a Thomson-Cox-Hastings pseudo-Voigt function. Refinement with the anisotropic line broadening procedure was used to estimate the anisotropy of the C–S–H coherent domains morphology.

2.2.2. Thermal analysis coupled with mass spectroscopy (TGA-MS)

The samples were studied by thermal analysis coupled with mass spectroscopy in order to quantify the water amounts and to detect the eventual carbonation. TGA analyses were performed on a Setaram TG92 apparatus. The powdered sample (about 10–15 mg) was introduced in an alumina crucible, measurements were realized from room temperature up to 1100 °C with a heating rate of 5 °C min^{-1} under air flow of 20 ml min^{-1}. A blank curve, obtained under the same conditions with the same empty alumina crucible, was systematically subtracted. A small part of the evacuated flux was analyzed by mass spectroscopy with a Thermostar Balzers instrument to follow the water and carbon dioxide releases.

3. Results and discussion

3.1. Sample chemical compositions

The experimental Ca/Si and Ca/(Si+Al) ratios were indirectly checked by chemical analysis of the solutions. Results (see Table 1) indicate that synthesized samples were very close to the nominal expected ratios for the C–S–H series, excepted for C–A–S–H_1.7 samples (i.e. the biphasic samples which contains about 7 wt% of portlandite). The experimental Ca/Si ratios from samples belonging to the C–A–S–H series were systematically below the expected value; namely for the high Ca/Si value (1.14 instead of 1.3 for C–A–S–H_1.3, 1.29 instead of 1.5 for C–A–S–H_1.5 and 1.36 instead of 1.7 for C–A–S–H_1.7). TGA analyses performed from room temperature up to 1100 °C allowed the determination of the water amounts (six thermogravimetric curves are shown in Fig. 2). All the TGA analyses showed extremely similar curves. Values were distributed between 1.5 (for C–A–S–H_1.0) and 2.1 (for C–S–H_1.5) water molecules per unit formulae, with a mean value of 1.7 (Table 1). Only sample C–S–H_0.8 exhibited a significantly smaller amount of water (1.0 water molecule per unit formula). The water content of C–S–H highly depends on the drying conditions: for a C–S–H with a Ca/Si ratio equal to 1.7 formed by hydration of C_3S and kept at 11% relative humidity, the average S/H ratio is around 2 [30], while the non-evaporable water corresponds to a S/H ratio between 1.3 and 1.5 [31]. Two different water releases could be differentiated during the heat treatment: a first relatively sharp release centered at about 120–150 °C and a broad release between 350 °C and up to 700–800 °C (from hydroxyl condensation). Small amounts of carbon dioxide were also detected in the flux evacuated during the TGA analyses. The small quantities and the temperature of release (below 300 °C) indicate weakly bonded carbonate anions probably surface physisorbed. That is the reason why they were not considered in the chemical composition given in Table 1.

3.2. Comparison of the structural models

Fig. 3 shows the twelve X-ray powder patterns. Poorly resolved powder patterns are characteristic of C–S–H phase. Samples with high Ca/Si ratios show the presence of a secondary calcic phase: portlandite $Ca(OH)_2$ in case of C–S–H_1.5 and C–S–H_1.7, and monocarboaluminate $Ca_4Al_2(OH)_{12} \cdot CO_3 \cdot 5H_2O$ [32,33] in case of C–A–S–H_1.7. The position of the first diffraction peak, close to $2\theta = 7^\circ$, gave indication on the basal spacing which decreased from about 14 Å ($2\theta = 6.4^\circ$) for C–S–H_0.8 to about 11.5 Å ($2\theta = 7.7^\circ$) for C–S–H_1.7. The powder patterns of C–A–S–H samples were less resolved. Nevertheless it is clear that basal spacings in C–A–S–H were higher than those in C–S–H. According to these observations on basal spacing, the structural models of tobermorite 14 Å, tobermorite 11 Å and jennite were first taken into account. The structural models of the less hydrated tobermorite 9 Å were not considered here. The nine tobermorite structural models compatible with our synthesized C–S–H phase (i.e. one tobermorite 14 Å model and eight tobermorite 11 Å models) and one jennite structural model were used to perform preliminary Rietveld refinements on X-ray powder patterns from the three C–S–H_0.8, C–S–H_1.1 and C–S–H_1.7 samples. These preliminary

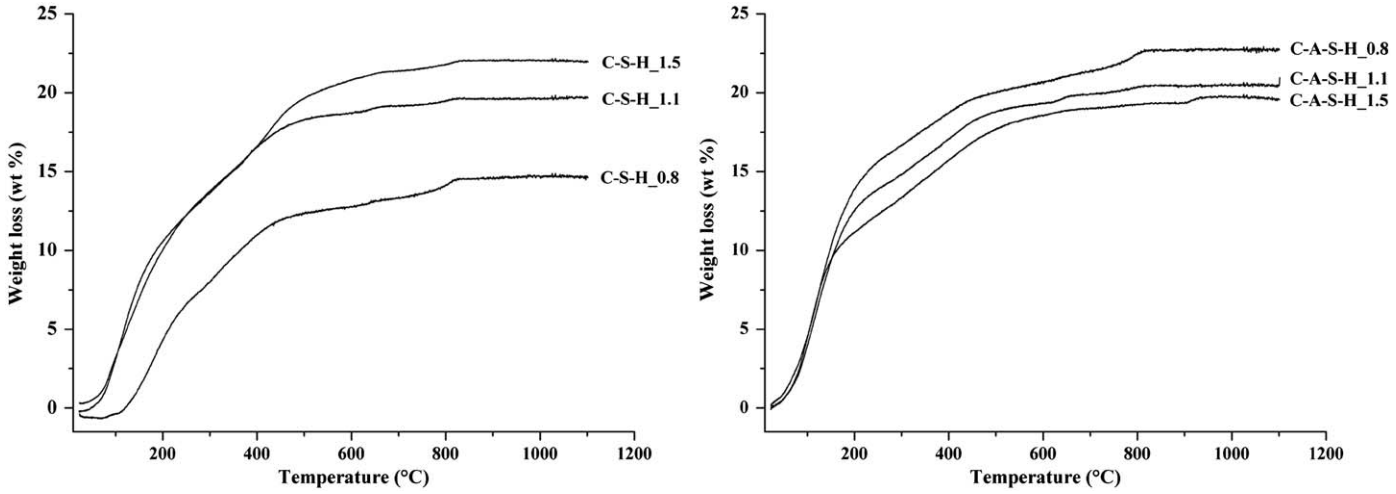

Fig. 2. Thermogravimetric curves from the six following samples: C–S–H_0.8, C–S–H_1.1 and C–S–H_1.5 (right), and C–A–S–H_0.8, C–A–S–H_1.1 and C–A–S–H_1.5 (left).

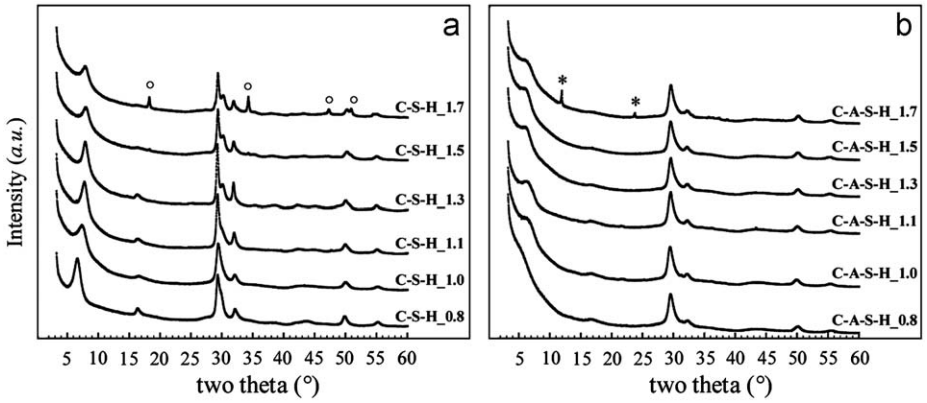

Fig. 3. X-ray powder patterns recorded with λ_{Cu}=1.5418 Å from the six C–S–H samples (a) and the six C–A–S–H samples (b). Circles and stars indicate, respectively, the presence of diffraction peaks from portlandite and monocarboaluminate phases.

Table 2
Comparison of the preliminary Rietveld refinement reliabilities (χ^2 values) for the 10 (nine tobermorite-types and one jennite-type) models compatible with the C–S–H phase.

Structural model	Space group	χ^2		
		C–S–H_0.8	C–S–H_1.1	C–S–H_1.7
Tobermorite 14 Å	*Cc*	~30	~50	~70
Tobermorite 11 Å Mdo1	*Fdd*2	10.4	17.3	15.7
Tobermorite 11 Å Mdo2	*Cm*	~50	~90	~100
Tobermorite O	*Imm*2	8.4	15.1	16.2
Tobermorite M	$P2_1$	8.4	11.0	14.2
Clinotobermorite	*C*2/*c*	~140	~150	~150
Clinotobermorite	*C*2/*m*	~90	~110	~110
Clinotobermorite	*CC*	~130	~150	~150
Clinotobermorite	*P*1	~130	~150	~150
Jennite	$P\bar{1}$	~160	~120	~90

refinements were performed on lattice parameters, line profile parameters, preferred orientation, asymmetry parameters and anisotropic crystal shape parameters. The atomic positions and site occupancies were not refined here. These preliminary refinements were performed on the three C–S–H_0.8, C–S–H_1.1 and C–S–H_1.7 samples in order to determine the best structural model to apply along the C–S–H series according to the Ca/Si value. Reliabilities of the preliminary Rietveld refinement are gathered in Table 2. From the 10 structural models checked, only three were compatible with our powder patterns: tobermorite 11 Å Mdo1, tobermorite O and tobermorite M. Whatever the observed basal spacing the tobermorite 14 Å model and jennite model did not allow refining correctly the powder pattern. Table 2 shows that one structural model was suitable for all the compositions (the tobermorite M model always allowed reaching the minimal χ^2 value) and thus indicates an apparent structural continuity within the C–S–H series. This model was previously used in the literature to refine powder patterns (with exclusion of the first diffraction line corresponding to the basal spacing) of C–S–H with low Ca/Si ratio [10]. The present work shows that it can be extended to the whole powder pattern, and to the whole C–S–H composition range. Therefore the tobermorite M model, monoclinic $P2_1$ symmetry, was further scrutinized.

3.3. Rietveld analyses of the C–S–H series

The six powder patterns from the C–S–H series (represented in Fig. 3a) was refined by using the tobermorite M model solved by Hamid [16]. The atomic labels designated by Hamid were used in the following, and the atomic coordinates were converted in the conventional $P2_1$ space group (using the $\vec{b}$ unique monoclinic axis). Fig. 1 shows general views of the structure with indication of the six calcium (labels Ca_L and Ca_I) and the six silicon (labels Si_P and Si_B) crystallographic sites. All structural and microstructural

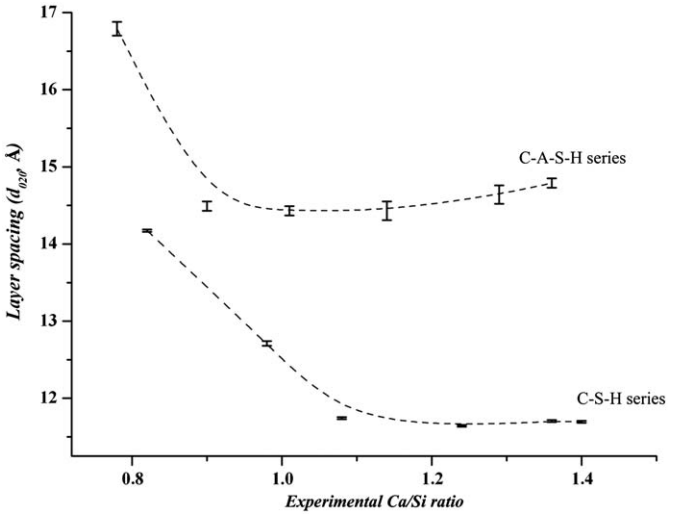

Fig. 4. Variation of the refined interlayer, d_{020}, distance versus the experimental Ca/Si ratio for the two C–S–H and C–A–S–H series.

parameters were refined (more of 40 refined parameters), except the atomic positions (because of the numerous 32 independent atomic sites and the largely unresolved diffraction lines). Refinement of the atomic coordinates would have introduced 96 supplementary parameters, which was not reasonable according to the low resolution of the X-ray powder patterns. This led to quite large, but acceptable for the following discussion, interatomic Si–O distances for the C–S–H_0.8 sample: average Si–O distances of 1.77 Å compare to 1.67 Å for C–S–H_1.0, 1.65 Å for C–S–H_1.1, 1.64 Å for C–S–H_1.3, C–S–H_1.5 and C–S–H_1.7, or 1.61 Å for quartz. The anisotropic average crystallite size was separated and refined from the sample intrinsic anisotropic line broadening. Site occupancies of calcium and silicon sites were allowed to vary in order to refine the Ca/Si ratio. Both Ca and Si positions were separated in two categories (i.e. Ca_L and Ca_I, for respectively, layer and interlayer Ca sites, and Si_P and Si_B, for respectively, paired and bridging Si sites). Each category was refined with a common occupancy (a total of four occupancy factors was used). The occupancy was fixed to unity, respectively, to zero when the refined value was close (i.e. in the standard deviation) to 1, respectively, 0. A shift parameter, Sh, (related to stacking faults [28,34–36]), corresponding to the displacement of certain groups of reflections, was refined according to the expression $2\theta_{shifted}=2\theta_{Bragg}+2\times10^{-2}\,Sh\,d^2\tan\theta$ for reflections ($h\,k\,0$) with $h+k=4n$. Values obtained during this work clearly differed from zero and thus characterized the existence of stacking faults in the layered structure of C–S–H. Fig. 4 shows the variation of the interlayer distance (d_{020}) versus the Ca/Si ratio. As already described in the literature [37] a decrease in the interlayer distance was first observed when the Ca/Si ratio increased (from 14.17 Å for C–S–H_0.8 down to 11.74 Å for C–S–H_1.1) and then became almost constant for higher Ca/Si ratio. In spite of the high d_{020} refined value for the low Ca/Si ratios (14.17 and 12.71 Å, for respectively, C–S–H_0.8 and C–S–H_1.0), the tobermorite M model (i.e. a tobermorite 11 Å model) allowed reaching accurate refinement (as represented in Fig. 5, and indicated by the conventional Rietveld reliability factors in Table 3). Structural continuity along the C–S–H series was evidenced from C–S–H_0.8 to C–S–H_1.7: the same structural model could be used to refine all the powder patterns by refining the lattice parameters and the cationic site occupancies. The unit cell volume continuously decreased when the Ca/Si ratio increased (a decrease close to 20% was observed over the whole

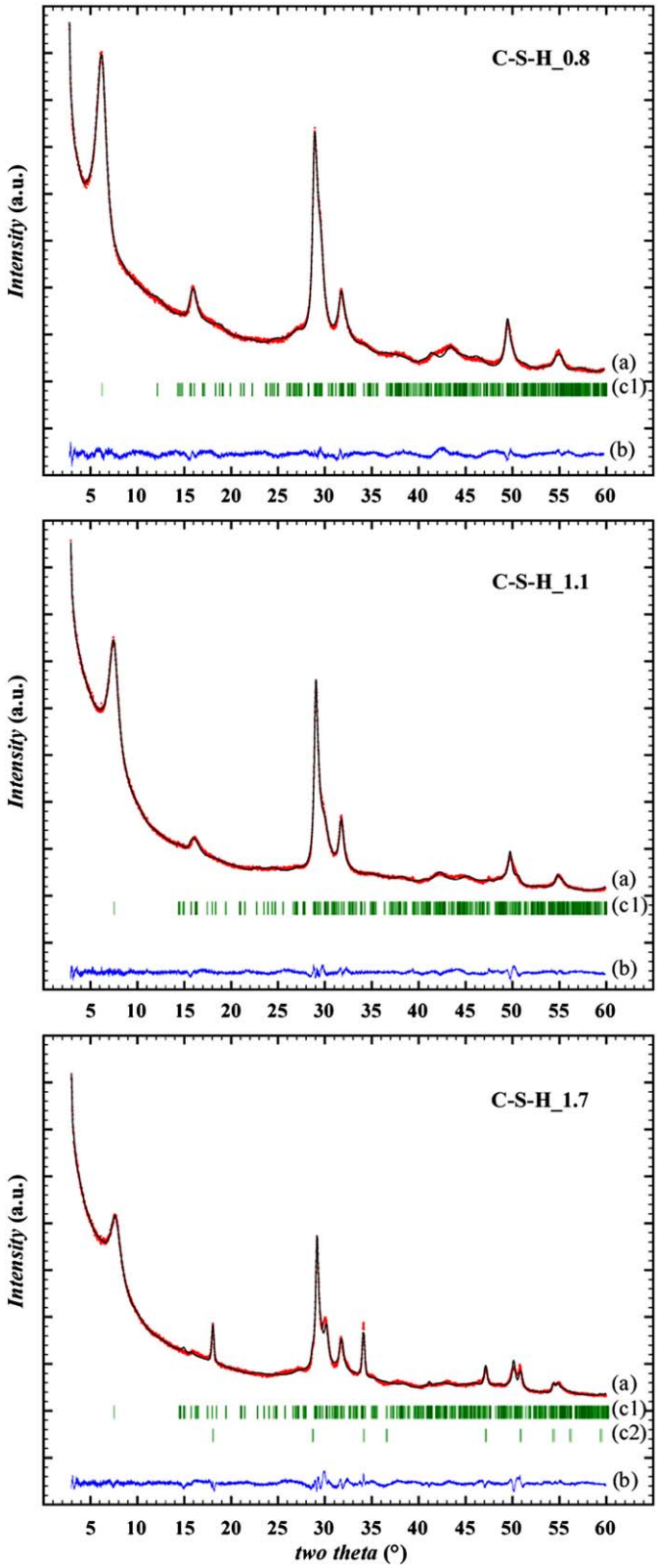

Fig. 5. Rietveld plots for samples C–S–H_0.8, C–S–H_1.1 and C–S–H_1.7: experimental (a, red markers) and simulated (a, continuous line) data, difference curves (b, blue curves) and Bragg peak positions for C–S–H and $Ca(OH)_2$ (respectively, c1 and c2, red markers). (For interpretation of the references to the color in this figure legend, the reader is referred to the web version of this article).

studied domain). The contraction of the layer spacing when increasing the Ca/Si ratio corresponded to the emptying of the bridging silicon tetrahedra (Si3 and Si5 sites) in a first step,

Table 3
Rietveld refinement results on the C–S–H series (standard deviations are indicated in parentheses).

C–S–H_n	n=0.8	n=1.0	n=1.1	n=1.3	n=1.5	n=1.7
χ^2[a]	4.51	3.69	4.37	7.04	6.28	6.45
Rp, Rwp[a]	0.059,0.069	0.069,0.078	0.080,0.089	0.103,0.110	0.130,0.137	0.134,0.141
a (Å)	7.356 (1)	7.305 (2)	7.3042 (9)	7.290 (1)	7.269 (1)	7.2474 (8)
b (Å)	28.347 (9)	25.41 (2)	23.482 (9)	23.284 (8)	23.41 (1)	23.40 (1)
c (Å)	6.754 (1)	6.731 (2)	6.7395 (9)	6.749 (1)	6.749 (1)	6.7300 (6)
β (°)	123.552 (5)	123.478 (5)	123.305 (4)	123.200 (4)	123.281 (5)	123.223 (5)
V (Å^3)	1173.6 (5)	1042 (1)	966.1 (4)	958.5 (4)	960.1 (5)	954.4 (5)
B_{iso} (Å^2)	0.77 (9)	1.5 (1)	2.0 (1)	0.8 (1)	1.6 (2)	0.9 (2)
Occ. (Ca_L)[b]	1 (–)	1 (–)	1 (–)	1 (–)	1 (–)	1 (–)
Occ. (Ca_I)[b]	0.31 (2)	0.12 (2)	0.10 (1)	0.18 (1)	0.31 (2)	0.32 (2)
Occ. (Si_B)[b]	0.59 (2)	0.18 (3)	0 (–)	0 (–)	0 (–)	0 (–)
Occ. (Si_P)[b]	1 (–)	1 (–)	1 (–)	0.94 (1)	0.86 (2)	0.83 (2)
Ca/Si[c]	0.89 (2)	0.97 (2)	1.05 (1)	1.16 (2)	1.34 (3)	1.40 (3)
Size$_{[100]}$ (Å)[d]	85	80	85	60	65	65
Size$_{[010]}$ (Å)[d]	40	35	50	55	55	55
Size$_{[001]}$ (Å)[d]	90	85	115	150	130	130
Sh[e]	−3.2 (3)	−2.7 (4)	−6.2 (2)	−5.9 (3)	−5.8 (3)	−7.3 (3)
$Ca(OH)_2$[f]	–	–	–	–	0.7 (1)	6.9 (2)

[a] Rietveld reliability factors.
[b] Occ. (Ca_L), Occ. (Ca_I), Occ. (Si_B) and Occ. (Si_P) are occupancy parameters of respectively calcium sites in the layer (Ca1, Ca2, Ca3 and Ca4 sites), interlayer calcium sites (Ca5 and Ca6 sites), bridging silicon sites (Si3 and Si5 sites) and paired silicon site (Si1, Si2, Si4 and Si6 sites).
[c] Refined Ca/Si ratio.
[d] Anisotropic size refinement allowed indicating the coherent domain size along the directions [100], [010] and [001].
[e] Shift parameter refined for ($h\,k\,0$) with $h+k=4n$.
[f] Refined amount of portlandite in weight percent (wt%).

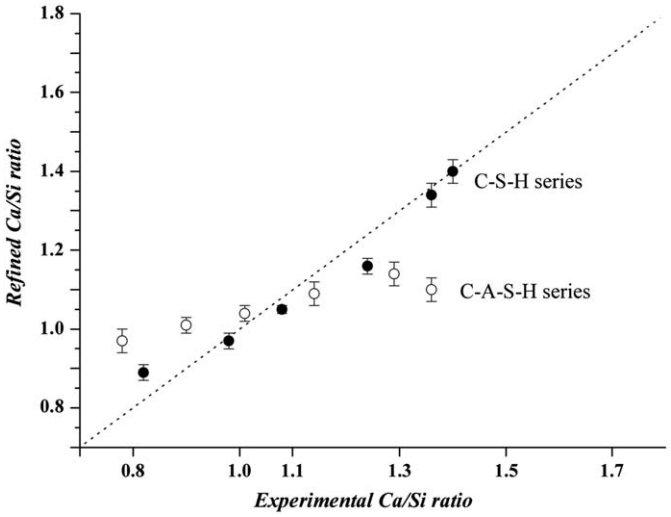

Fig. 6. Refined Ca/Si ratio versus experimental Ca/Si ratio (full circles for the C–S–H series and open circles for the C–A–S–H series). Dotted line shows the ideal segment.

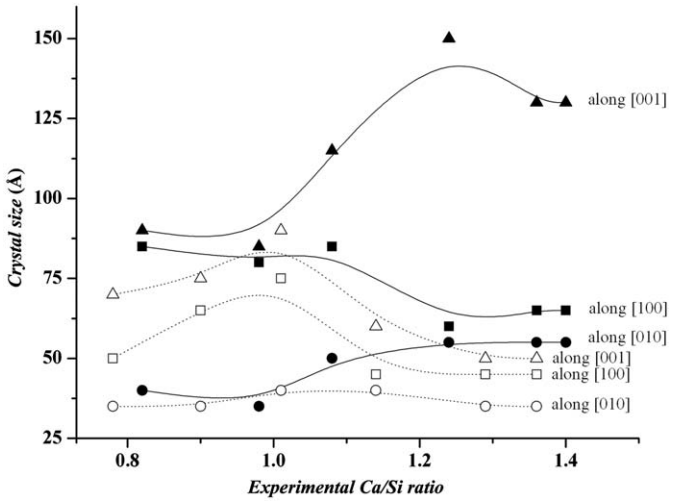

Fig. 7. Coherent domain sizes along the main [100] (squares), [010] (circles) and [001] (triangles) directions versus the experimental Ca/Si ratio for the C–S–H series (full symbols, full lines) and for the C–A–S–H series (open symbols, dotted lines). Lines are just guides for the eyes.

followed by a decrease in the occupancies of the paired silicon tetrahedra (Si1, Si2, Si4 and Si6 sites). Occupancies of the two bridging Si3 and Si5 sites reached zero for C–S–H_1.1, afterward the occupancies of the paired silicon tetrahedra (Si1, Si2, Si4 and Si6 sites) started to decrease (0.94 for C–S–H_1.3) to reach 0.84 for C–S–H_1.7. The occupancies of the interlayer calcium sites (Ca5 and Ca6) decreased from 0.36 for C–S–H_0.8 to 0.10 for C–S–H_1.1 (i.e. corresponding to the large decrease in the interlayer distance). From C–S–H_1.3 the occupancies of these two calcium sites increased to reach the value 0.31 for C–S–H_1.5 and C–S–H_1.7 (i.e. corresponding to the almost constant d_{020} value close to 11.70 Å). These refined cation occupancies agreed fairly well with the progressive transition from the C–S–H(I) description (with infinite polymerized silicate chains involving bridging Si tetrahedra) to the C–S–H(II) description (with isolated dimers of paired Si tetrahedra). Refined Ca/Si ratios were in quite good agreement with the nominal ratios (Fig. 6). Weak discrepancy between refined and experimental ratios should be explained by the fact that the interlayer water amount was kept constant during the refinement of all the powder patterns (in order to have stable and reliable refinements). The small crystallite size inferred from the microstructural parameters (see Table 3) was in fairly good agreement with values mentioned in the literature [10,11,38–40]. C–S–H was formed of platy-shaped crystals (a short dimension along the monoclinic $\vec{b}$ axis, and two larger dimensions along $\vec{a}$ and $\vec{c}$) when bridging silicon tetrahedra

were present. Crystallites in C–S–H_0.8 and C–S–H_1.0 samples were flattened along the monoclinic $\vec{b}$ direction. The crystal shape became fibrous (elongated along the $\vec{c}$ direction), as usually observed in hydrated cement pastes, since the bridging silicon tetrahedra disappeared. TEM micrographs realized by Richardson [11,38,41] gave experimental illustrations of the platy morphology of C–S–H for low Ca/Si ratios and fibrous morphology for higher Ca/Si ratios. The variation of the morphology anisotropy of C–S–H crystals (from platy to acicular when the Ca/Si ratio increased) is represented in Fig. 7. The crystallite dimension along the stacking direction was around 50 Å whatever the Ca/Si ratio.

3.4. Rietveld analyses of the C–A–S–H series

X-ray powder patterns from C–A–S–H samples (Fig. 3b) showed a decrease in the coherent domain size and an increase in the layer spacing when introducing aluminum atoms into C–S–H phase [42]. The first diffraction line, characteristic of the layer spacing, was largely shifted toward the low 2θ-angles, as well as broadened and weakened for C–A–S–H samples as compared to C–S–H samples. Rietveld refinement results (gathered in Table 4, see also Fig. 4) agreed with these observations. Microstructural refined parameters (represented in Fig. 7) illustrate the smaller crystallite dimensions in the C–A–S–H series as compared to the previously described C–S–H series. The platy- or fibrous-shaped crystals were not observed in the C–A–S–H series as the three main directions showed short dimensions (between 35 and 75 Å). The insertion of aluminum in C–S–H structure involves a decrease in the coherent domain size (compare Tables 3 and 4) which is observed along the three crystallographic axes, and is more pronounced for high Ca/Si values. According to the aluminum inserted amount in C–S–H, two types of morphology have been previously observed by TEM imaging (fibrous for low Al amount and small Ca/(Si+Al) ratio, and platy for higher Al amount and high Ca/(Si+Al) ratio) [43]. The layer spacing increased of about 2 Å when introducing low amount of aluminum (Al/Si atomic ratio of 0.1 only). The presence of supplementary interlayer water molecules cannot be responsible for such an increase in the layer spacing due to the quite constant amount of water observed for the different samples (Table 1). The refinement of the Ca and Si sites occupancies was performed. The refined occupancies show that the tobermorite M model cannot describe accurately the structure of C–A–S–H samples (Table 4 and Fig. 6). This result gives indication of a deep structural modification, in the interlayer part of the C–S–H structure, when aluminum atoms are inserted. We were not able to locate Al atoms in the C–A–S–H structure by long-range order investigation, but the results highlight the fact that Al atoms are not simply substituted to Si atoms. These observations give evidence for the location of inserted Al atoms in their own crystallographic sites. A layer spacing increase of about 2 Å is enough to allow the insertion of a new hydroxide layer (of aluminum, or calcium, or both as an AFm-type layer) between the silicate entities at the center of the interlayer region of the C–S–H structure. Unlike the C–S–H series, the layer spacing in the C–A–S–H series was the shortest for the C–A–S–H_1.0, C–A–S–H_1.1 and C–A–S–H_1.3 samples (while it increased, slightly for C–A–S–H_1.5 sample, and more for C–A–S–H_1.7 sample). Aluminum atoms seem to play their own crystallographic part when inserted into the C–S–H structure, which is not a simple substitution to Si atoms.

4. Conclusion

Rietveld refinements performed on X-ray powder patterns from samples belonging to the C–S–H series highlight the structural continuity from Ca/Si=0.8 (i.e. the C–S–H(I) type) up to Ca/Si=1.7 (i.e. the C–S–H(II) type). The tobermorite M model [17] was used to accurately refine the powder patterns of all the synthesized C–S–H samples. Structural continuity, or smooth steady structural changes, involves both lattice parameters (with a large decrease in the unit cell volume for the low Ca/Si values when passing from the C–S–H(I) type to the C–S–H(II) type around the Ca/Si value of 1.0) and cation distribution (evolution of the site occupancies of the four structurally different cations, i.e. Ca_I, Ca_L, Si_B and Si_P sites, which explains the continuous changes from the C–S–H(I) type to the C–S–H(II) type when the

Table 4
Rietveld refinement results on the C–A–S–H series (standard deviations are indicated in parentheses).

C–A–S–H_*n*	*n*=0.8	*n*=1.0	*n*=1.1	*n*=1.3	*n*=1.5	*n*=1.7
χ^2[a]	9.5	12.0	9.3	11.0	11.9	7.3
*R*p, *R*wp[a]	0.159,0.166	0.185,0.180	0.136,0.154	0.163,0.171	0.167,0.169	0.118,0.135
a (Å)	7.290 (3)	7.313 (3)	7.293 (3)	7.283 (3)	7.280 (3)	7.273 (1)
b (Å)	33.59 (5)	28.97 (3)	28.85 (3)	28.86 (7)	29.29 (7)	29.59 (4)
c (Å)	6.626 (2)	6.655 (2)	6.640 (2)	6.633 (3)	6.632 (3)	6.641 (1)
β (°)	123.11 (2)	123.20 (2)	123.10 (2)	123.08 (1)	123.10 (1)	122.92 (1)
V (Å^3)	1359 (2)	1180 (1)	1170 (1)	1168 (3)	1185 (3)	1200 (2)
B_{iso} (Å^2)	3.2 (3)	2.0 (1)	2.8 (1)	2.4 (1)	2.0 (1)	2.4 (2)
Occ. (Ca_L)[b]	1 (–)	1 (–)	1 (–)	1 (–)	1 (–)	1 (–)
Occ. (Ca_I)[b]	0.59 (3)	0.49 (2)	0.53 (2)	0.39 (3)	0.45 (3)	0.48 (3)
Occ. (Si_B)[b]	0.68 (3)	0.47 (2)	0.44 (2)	0.20 (3)	0.15 (3)	0.26 (3)
Occ. (Si_P)[b]	1 (–)	1 (–)	1 (–)	1 (–)	1 (–)	1 (–)
Ca/Si[c]	0.97 (3)	1.01 (2)	1.04 (2)	1.09 (3)	1.14 (3)	1.10 (3)
$Size_{[100]}$ (Å)[d]	50	65	75	45	45	45
$Size_{[010]}$ (Å)[d]	35	35	40	40	35	35
$Size_{[001]}$ (Å)[d]	70	75	90	60	50	50
$C_4A\bar{C}H_{11}$[e]	–	–	–	–	–	5.1 (2)

[a] Rietveld reliability factors.
[b] Occ. (Ca_L), Occ. (Ca_I), Occ. (Si_B) and Occ. (Si_P) are occupancy parameters of respectively calcium sites in the layer (Ca1, Ca2, Ca3 and Ca4 sites), interlayer calcium sites (Ca5 and Ca6 sites), bridging silicon sites (Si3 and Si5 sites) and paired silicon site (Si1, Si2, Si4 and Si6 sites).
[c] Refined Ca/Si ratio.
[d] Anisotropic size refinement allowed indicating the coherent domain size along the directions [100], [010] and [001].
[e] Refined amount of monocarboaluminate in weight percent (wt%).

Ca/Si ratio increases). Refinement results indicate that the term 'defect tobermorite M' model is much more appropriate than the terms 'tobermorite/jennite' or 'tobermorite/portlandite' models to describe the crystal-chemistry of C–S–H (see Richardson [11] for a comprehensive review of the successive proposed structural models for C–S–H). The continuous change is also observed in terms of morphology of the coherent domains; evolution occurs from platy to fibrous nano-domains. C–S–H phase appears to be nano-crystallized materials: a well ordered structure combined with a small coherent domain size (in the range 50–100 Å). This 'nano-crystallized' feature contrasts with the generally attributed 'poorly ordered phase' description for C–S–H. The insertion of a small amount of aluminum atoms in the C–S–H structure (i.e. the C–A–S–H series synthesized with an Al/Si ratio of 0.1) disrupts the framework organization. The continuity, or the steady change, in the C–A–S–H series is not lost, but some structural parameters are, however, not accurately refined by using the same tobermorite M model (giving rise to incorrect nominal cation composition and localization, certainly due to aluminum cation positions, when adopting similar refinement procedure as for C–S–H series). The refined cationic site occupancies did not allow to access to the nominal composition of the C–A–S–H phases, namely for high Ca/(Si+Al) values underlining that the uptake of Al^{3+} cation within C–S–H is not straightforward since it is not arising simply from a substitution neither of the Ca^{2+} sites nor of the Si^{4+} sites. Localization of aluminum atoms in the structure was not allowed and the origin of the large increase in the layer spacing (about 2 Å for the C–A–S–H series) is not explained by the present long-range order investigation. Supplementary spectroscopic analyses (NMR spectroscopy and Raman spectroscopy) have been performed on the same samples to unravel the mechanism of insertion of Al atoms into the C–S–H structure to form the C–A–S–H phases [44].

References

[1] H. Le Chatelier, C.R. Acad. Sci. Paris 94 (1882) 867–869.
[2] W.S. Michaëlis, Z. Chem. Ind. Kolloide 5 (1909) 9–22.
[3] H. Le Chatelier, Trans. Faraday Soc. 14 (1919) 8–11.
[4] S.B. Newberry, M.M. Smith, J. Soc. Chem. Ind. 22 (1903) 94–95.
[5] G.A. Rankin, Trans. Faraday Soc. 141 (1919) 23–28.
[6] R.H. Bogue, The Chemistry of Portland Cement, second ed., Reinhold, New York, 1955.
[7] J.D. Bernal, J.W. Jeffery, H.F.W. Taylor, Mag. Concr. Res. 4 (1952) 49–54.
[8] H.F.W. Taylor, J. Chem. Soc. (1950) 3682–3690.
[9] J.A. Gard, H.F.W. Taylor, Cem. Concr. Res. 6 (1976) 667–677.
[10] A. Nonat, Cem. Concr. Res. 34 (2004) 1521–1528.
[11] I.G. Richardson, Cem. Concr. Res. 38 (2008) 137–158.
[12] H.D. Megaw, C.H. Kelsey, Nature 177 (1956) 390–391.
[13] H.F.W. Taylor, J.W. Howison, Clay Miner. Bull. 3 (1956) 98–111.
[14] H.F.W. Taylor, J. Am. Ceram. Soc. 69 (1986) 464–467.
[15] E. Bonaccorsi, S. Merlino, A.R. Kampf, J. Am. Ceram. Soc. 88 (2005) 505–512.
[16] S. Merlino, E. Bonaccorsi, T. Armbruster, Eur. J. Miner. 13 (2001) 577–590.
[17] S.A. Hamid, Zeit. Krist. 154 (1981) 189–198.
[18] S. Merlino, E. Bonaccorsi, T. Armbruster, Am. Miner. 84 (1999) 1613–1621.
[19] S. Merlino, E. Bonaccorsi, T. Armbruster, Eur. J. Miner. 12 (2000) 411–429.
[20] C. Hoffmann, T. Armbruster, Zeit. Krist. 212 (1997) 863–873.
[21] X. Cong, R.J. Kirkpatrick, Advn. Cem. Bas. Mat. 3 (1996) 144–156.
[22] X. Cong, R.J. Kirkpatrick, Advn. Cem. Bas. Mat. 3 (1996) 133–143.
[23] I.G. Richardson, Cem. Concr. Res. 29 (1999) 1131–1147.
[24] F. Brunet, Ph. Bertani, Th. Charpentier, A. Nonat, J. Virlet, J. Phys. Chem. B 108 (2004) 15494–15502.
[25] J. Skibsted, M.D. Andersen, H.J. Jakobsen, Zem. Kalk Gips Int. 60 (2007) 70–83.
[26] J. Skibsted, C. Hall, Cem. Concr. Res. 38 (2008) 205–225.
[27] X. Chen, I. Pochard, A. Nonat, in: Proceedings of the 12th International Congress of Chemistry of Cement, Montreal, 2007.
[28] J. Rodriguez-Carvajal, PROGRAM FullProf.2k—version 3.20, Laboratoire Léon Brillouin (CEA-CNRS), France, 2005 (FullProf.2k manual available on 〈http://www-llb.cea.fr/fullweb/fp2k/fp2k_divers.htm〉).;
See also J. Rodriguez-Carvajal, T. Roisnel, Mater. Sci. Forum 123 (2004) 443–444.
[29] E. Bonaccorsi, S. Merlino, H.F.W. Taylor, Cem. Concr. Res. 34 (2004) 1481–1488.
[30] H.F.W. Taylor, Cement Chemistry, second ed., Thomas Telford Publishing, New York, 1997.
[31] L.E. Copeland, J.C. Hayes, ASTM Bull. 194 (1953) 70–74.
[32] M. François, G. Renaudin, O. Evrard, Acta Cryst. C 54 (1998) 1214–1217.
[33] G. Renaudin, M. François, O. Evrard, Cem. Concr. Res. 29 (1999) 63–69.
[34] E.J. Mittemeijer, P. Scardi, in: Diffraction analysis of the microstructure of materials, Springer Series in Materials Science, vol. 68, Springer, Berlin, 2004.
[35] B.E. Warren, X-Ray Diffraction, Dover, New York, 1990.
[36] S. Gomes, G. Renaudin, H. Hagemann, K. Yvon, M.P. Sulic, C.M. Jensen, J. Alloys Compd. 390 (2005) 305–313.
[37] I. Klur, B. Pollet, J. Virlet, A. Nonat, in: A.-R. Grimmer, H. Zanni, P. Sozzani (Eds.), Nuclear Magnetic Resonance Spectroscopy of Cement Based Materials, Springer, Berlin, 1998.
[38] I.G. Richardson, Cem. Concr. Res. 34 (2004) 1733–1777.
[39] S. Gauffinet, E. Finot, E. Lesniewska, A. Nonat, C.R. Acad. Sci. Paris 327 (1998) 231–236.
[40] C. Plassard, E. Lesniewska, I. Pochard, A. Nonat, Ultramicroscopy 100 (2004) 331–338.
[41] I.G. Richardson, in: P. Barnes, J. Bensted (Eds.), Structure and Performance of Cements, second ed., Spon Press, London, 2002, pp. 500–556 Chapter 22.
[42] X. Chen, Ph.D. Thesis, Université de Bourgogne, Dijon, 2007.
[43] J. Russias, F. Frizon, C. Cau-Dit-Coumes, A. Malchère, T. Douillard, C. Joussot-Dubien, J. Am. Ceram. Soc. 91 (2008) 2337–2342.
[44] G. Renaudin, J. Russias, F. Leroux, C. Cau-dit-Coumes, F. Frizon, J. Solid State Chem., in press, doi:10.1016/j.jssc.2009.09.024.